

Article

# Joint Inversion of Sea Surface Wind and Current Velocity Based on Sentinel-1 Synthetic Aperture Radar Observations

Jingbei Sun <sup>1,2</sup>, Huimin Li <sup>1,2</sup>, Wenming Lin <sup>1,2,\*</sup> and Yijun He <sup>1,2</sup>

<sup>1</sup> School of Marine Sciences, Nanjing University of Information Science and Technology, Nanjing 210044, China; 20211209010@nuist.edu.cn (J.S.); huimin.li@nuist.edu.cn (H.L.); yjhe@nuist.edu.cn (Y.H.)

<sup>2</sup> Key Laboratory of Space Ocean Remote Sensing and Application, Ministry of Natural Resources, Beijing 100081, China

\* Correspondence: wenminglin@nuist.edu.cn

**Abstract:** Spaceborne synthetic aperture radar (SAR) has been proven to be a useful technique for observing the sea surface wind and current over the open ocean given its all-weather data-gathering capability and high spatial resolution. In addition to the commonly used radar return magnitude quantified by normalized radar cross section (NRCS), the Doppler centroid anomaly (DCA) has added another dimension of information. In this study, we combine the NRCS and DCA for a joint inversion of wind and surface current information using a Bayesian method. SAR-estimated Doppler is corrected by a series of steps, including the removal of scalloping effect and land correction. The cost function of this inversion scheme is constructed based on NRCS, DCA, and a background model wind. The retrieved wind results show the quality of performance through comparison with the in situ buoy measurements, showing a mean bias and a root-mean-square error (RMSE) of 0.33 m/s and 1.45 m/s for wind speed and 6.94° and 35.74° for wind direction, respectively. The correlation coefficients for wind speed and direction reach 0.931 and 0.661, respectively. Based on the obtained wind field, the line-of-sight velocity of the sea surface current is then derived by removing the wind contribution using the empirical model. The results show a consistent spatial pattern relative to the high-frequency radars, with the comparison relative to the drifter-measured current velocity exhibiting a mean bias of 0.02 m/s and RMSE of 0.32 m/s, demonstrating the reliability of the proposed inversion scheme. Such results will serve as a prototype for future spaceborne sensors to combine the radar return and Doppler information for the joint retrieval of wind vector and surface current velocity. This technique could be readily extended to the radar configuration of rotating beams for monitoring winds and current vectors.

**Keywords:** synthetic aperture radar (SAR); Doppler centroid anomaly; Bayesian method; wind and current velocity inversion



**Citation:** Sun, J.; Li, H.; Lin, W.; He, Y. Joint Inversion of Sea Surface Wind and Current Velocity Based on Sentinel-1 Synthetic Aperture Radar Observations. *J. Mar. Sci. Eng.* **2024**, *12*, 450. <https://doi.org/10.3390/jmse12030450>

Academic Editors: Lev Shemer, Anatoly Gusev, Ilaria Ferrando and Andrea Lira Loarca

Received: 8 December 2023

Revised: 26 February 2024

Accepted: 29 February 2024

Published: 2 March 2024



**Copyright:** © 2024 by the authors. Licensee MDPI, Basel, Switzerland. This article is an open access article distributed under the terms and conditions of the Creative Commons Attribution (CC BY) license (<https://creativecommons.org/licenses/by/4.0/>).

## 1. Introduction

The dynamics of the atmosphere and ocean are significantly influenced by ocean surface wind and currents. Ocean surface wind not only acts as a primary force driving the creation of surface waves but also plays a pivotal role in shaping the broader patterns of global ocean circulation. Concurrently, ocean currents serve as vital conduits, transporting heat, salinity, and nutrients, thereby exerting a profound impact on both climate and marine biology. Observations of sea surface current and winds are essential for understanding the air-sea interaction [1,2]. Despite their high accuracy, in situ measurements are limited by fixed spatial locations and by the great expenses and risks associated with the use of the instruments [3]. Over the past decades, the great advancements in spaceborne remote sensing have made it an invaluable source of measurements for the observation of the geophysical variables across the global ocean. Among these, microwave active radars have gained particular attention given their capability in collecting data under all kinds of weather conditions during day and night.

Wind field is the most basic atmospheric variable over the open ocean surface. The spaceborne scatterometer is to date the most widely used instrument for observing the sea surface wind. Such a radar measures the backscattering, often termed as normalized radar cross section (NRCS and  $\sigma^0$  used interchangeably throughout the text), that is not only related to radar configurations (radar wavelength, polarization, incidence angle), but also to the sea surface state (wind, waves, temperature and current et al.) [4]. For an inversion scheme of wind vector from the radar measurements, the empirical geophysical model function (GMF) associating NRCS and the radar parameter as well as the surface states is required. Note that each GMF is dedicated to a particular polarization and particular radar wavelengths [5]. The typical configuration of a scatterometer with multiple fixed beams or a rotating beam allows the sensor to independently resolve a unique wind vector based on a Bayesian scheme. To date, scatterometer-retrieved wind fields have been reported with an accuracy of 1.5 m/s and 20° for the wind speed and direction, respectively. These wind products are now routinely distributed to help monitor the spatial pattern of ocean winds, wave fields, weather forecasting, and ocean and atmospheric research, to name a few. Yet, the relatively coarse resolution of the scatterometer wind data at around 12.5 to 25 km has significantly limited its application in fine-resolution scenarios, like the rapidly changing winds across an atmospheric front or over coastal regions [6]. The other variable, ocean surface current, is as yet unresolved from the point view of remote sensing [7]. Radar altimeters that measure the sea surface height are able to obtain current fields in combination with geostrophic equilibrium relationships. This kind of technique is better than the use of in situ instruments in terms of the extended coverage, high accuracy, and shorter revisit period. It should be noted that the altimeter products are available at a spatial scale larger than 100 km; they are incapable of resolving fine-scale geophysical processes. In addition to that, the challenges of radar altimeters are the long revisit temporal period and extended gap distance between adjacent tracks. However, such situations have been alleviated by merging multiple altimeter satellites to achieve a relatively shorter revisit time and greater coverage [8].

Another popular remote-sensing instrument to observe the sea surface wind and current is synthetic aperture radar (SAR), which has a higher spatial resolution. In addition to the traditional NRCS magnitude, it adds another dimension of Doppler information [9]. As with to the scatterometer, sea surface wind data can also be obtained from SAR observations. However, SAR has only one incident radar beam, making it difficult to attain near-surface wind vectors without external inputs. A couple of methods have been proposed to deal with the resolution of wind vectors independently from SAR observations. Horstmann et al. [10] take advantage of the wind streak features directly extracted from SAR images to approximate the wind direction for the inversion of the wind speed. However, not all SAR images are present with streaks [11]. In addition, the Doppler information is used as an extra variable in the wind inversion scheme [12]. The Doppler centroid anomaly (DCA) represents the difference in satellite-measured Doppler and the predicted Doppler associated with the instrument attitude. This DCA, with a series of corrections, corresponds to the geophysical sea surface motion. Such a principle was first demonstrated in [13], exhibiting a simple model relating Doppler velocity to surface wind and current velocity. The steps to correct the DCA to obtain the geophysical components are detailed in [14] and later applied over the Agulhas Current region [15]. Kang et al. [16] analyzed the DCA data based on Radarsat-2 wide swath under tropical cyclones, which shows that DCA has positive and negative opposite values on both sides of the center of the tropical cyclone. Ever since then, over the past years, the potential of DCA to obtain wind and current velocity has gained growing attention [17,18].

Taking advantage of Sentinel-1 products acquired over the coastal regions, we explore the capability of combining NRCS and DCA information to jointly retrieve sea surface wind field and surface current velocity in this study. The correction algorithm of DCA from Sentinel-1 level-2 products, including the scalloping effect, is detailed here. The rest of this paper is organized as follows. Section 2 gives the data and method to implement the

overall processing flow, along with the GMFs included in this paper. Section 3 presents the processing chain and the inversion scheme as well as the validation of retrieved winds and current velocity. The Summary follows in Section 4.

## 2. Data and Method

### 2.1. Sentinel-1

Sentinel-1 (S-1) is a part of the European Space Agency's (ESA) Copernicus program, dedicated to Earth observation. Sentinel-1 carries an advanced SAR system that provides high-resolution radar imagery regardless of weather conditions or daylight. It is composed of two satellites (A and B, launched in 2014 and 2016, respectively. The Sentinel-1B mission ended in 2022), both operating at C band with a radar frequency of 5.405 GHz. S-1 is designed to operate at four imaging modes: interferometric wide swath (IW), extra wide swath, stripmap, and wave mode. IW acquisitions are mostly located along the coastal regions, with a swath of 250 km at the spatial slant-range spacing of 2.5 m by 15 m (range by azimuth) for the original single-look images.

In this study, the level-2 ocean (OCN) products of IW mode are included to jointly retrieve the sea surface wind and surface current velocity. This type of product is formatted into three components: ocean wind (OWI), radial velocity (RVL), and ocean swell [19]. Specifically, radar NRCS from the OWI component at a spatial resolution of  $1 \text{ km} \times 1 \text{ km}$  is used in the following analysis. The SAR-estimated Doppler centroid annotated in the RVL group is also included, available at  $1 \text{ km} \times 1 \text{ km}$  resolution. The products acquired by both satellites between January 2018 and December 2023 over the coast of North America are explored, resulting in the acquisition of 407 images. Figure 1 presents the spatial coverage of the S-1 IW products used in this study. Due to the revisit planning of S-1, all products are acquired over the overlapping coverage as shown. It is of note that all products are used for wind inversion and validation, while only SAR images over the Gulf Stream are included for current validation.

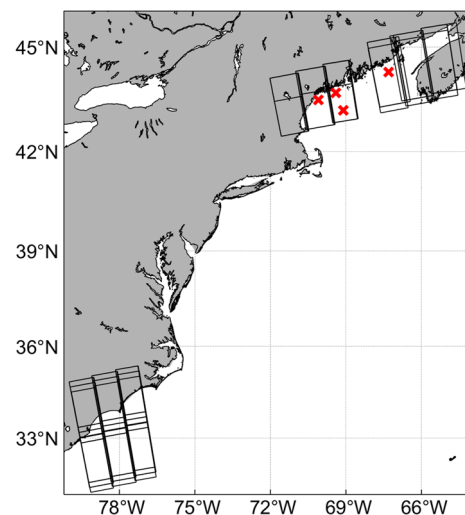


**Figure 1.** Spatial coverage of SAR images included in this study and the buoy locations used for wind inversion validation (marked by the red 'x' with buoy ID annotated).

### 2.2. ECMWF Winds

The wind vector from the European Center for Medium-Range Weather Forecasts (ECMWF) is used as the background wind for inversion. This product has undergone optimization through the assimilation of satellite observations and diverse observational data [20]. The wind vector is available at a spatial resolution of  $0.125^\circ \times 0.125^\circ$  every 6 h. This precision ensures that the wind speed and direction can be monitored with high accuracy at any location and time globally. In this study, the collocation criterion between SAR and ECMWF wind is the nearest in space and in time. It should be pointed out that

we use the ECMWF winds annotated in the S-1 level-2 OCN products for simplicity in this study.

### 2.3. Buoy Winds

In this paper, we use the wind vectors measured by the National Data Buoy Center (NDBC) buoys as a reference data source to validate the retrieved winds from SAR observations. Note that the majority of NDBC anemometers record wind speeds at an elevation of 2.5–4 m above the sea surface. In order to align with SAR-measured neutral winds at 10 m, all buoy wind speeds are converted to 10 m neutral winds. This conversion is carried out using a log-profile relationship based on the assumption of a neutrally stable boundary layer. The reference height is set as 10 m, and the sea surface roughness length is 0.0002 m with a negligible temperature gradient. For the remainder of this paper, the wind speed refers to the neutral wind speed at a height of 10 m unless explicitly stated and denoted as  $U_{10}$ . Given the limited coverage of SAR images, four buoys are finally chosen as shown in Figure 1 to provide wind data for validation. The closest wind pixels to the buoy locations are used in space, and the temporal collocation criterion is a duration of less than 30 min.

### 2.4. High-Frequency Radar

To further evaluate the performance of retrieved sea surface current velocity, the current velocity obtained by high-frequency radar (HF radar) is chosen as a reference dataset. The observational accuracy of HF radar has been reported to be in the order of 10 cm/s for the speed and 10 degrees for the direction. In this study, we used the HF radar products distributed by the National Oceanic and Atmospheric Administration (NOAA). The velocity field is available on an hourly basis with a spatial spacing of 6 km. The HF radar measures the average velocity within the upper 10 cm below the sea surface, which can be considered approximate to the SAR-observed radial current velocity at the very surface. The collocation criterion between the HF radar products and SAR observations is a duration of 3 h in time for qualitative comparison.

### 2.5. Drifter Current Velocity

In addition to the HF radars, we also included the current velocity measured by the surface drifters obtained within the framework of the global drifter program (GDP). Details can be found on the website <https://www.aoml.noaa.gov/global-drifter-program/> (accessed on 10 November 2023) and products are introduced in [21]. Drifters measure surface current velocity through the principle of Lagrangian drift. As the drifter moves with the ocean currents, its trajectory and speed are tracked via satellite-based positioning systems. By analyzing the drifter position changes over time, the surface current velocity and direction are then deduced. This Lagrangian approach offers a unique perspective, directly measuring the water movement rather than inferring it from Eulerian measurements at fixed locations. In this study, we use the 1-hourly interpolated ocean current velocity provided by the GDP products. The collocation criteria between SAR observations and the drifter measurements are a distance of 1 km in space and a temporal duration of 3 h.

### 2.6. CMOD7 and CDOP

Developed for global applications and implemented on the C-band advanced scatterometer (ASCAT), the empirical GMF known as CMOD7 has surpassed its predecessor CMOD5.N with higher wind retrieval accuracy [22]. This model covers a valid incidence angle range from 18° to 60°, well consistent with the incidences of S-1 IW images. CMOD7 establishes a relationship between NRCS, incidence angle, wind speed, wind direction (relative to radar line of sight), and polarization under neutral atmospheric stability, as defined by the following equation:

$$\sigma^0 = B_0[1 + B_1\cos(\phi) + B_2\cos(2\phi)] \quad (1)$$

where  $\phi$  represents the wind direction concerning the antenna look angle.  $B_0$  determines the NRCS level for a specific wind speed, while  $B_1$  and  $B_2$  describe the upwind/downwind and upwind/crosswind asymmetry of NRCS, respectively. All these three terms can be expressed as functions of incidence angle, wind speed, and wind direction [22].

Assuming corrected DCA information after a series of steps, the geophysical DCA can be still considered as the combination of sea state and sea surface current [13]. As such, the sea-state contribution should be removed to obtain a clean current velocity. The C-band Doppler model (CDOP) is designed to achieve such a purpose by building the relationship of DCA with respect to the radar configuration and sea surface wind field [12]. This model takes the form of

$$f^{DA} = CDOP(U_{10}, \varphi_w, \theta, pol) \tag{2}$$

where  $U_{10}$  and  $\varphi_w$  are the wind speed and direction (relative to the radar looking direction) at a height of 10m, respectively,  $\theta$  is the incidence angle, and  $pol$  is the polarization mode of radar. The function form and values of each coefficient are detailed in [12].

### 2.7. Method

SAR-estimated Doppler centroid  $f_{Dc}$  provided in the level-2 OCN product is associated with the relative motion between the radar sensor and the target. In the case of sea surface,  $f_{Dc}$  is influenced not only by the relative motion between the Earth and the satellite, but also by the surface currents and wind and wave fields. It can be decomposed into the following components:

$$f_{Dc} = f_{Dp} + f_{em} + f_{sca} + f_{cur} + f_w \tag{3}$$

where  $f_{Dp}$  is the predicted (geometric) Doppler frequency,  $f_{em}$  is the antenna electronic miss-pointing term,  $f_{sca}$  is the scalloping signal term,  $f_{cur}$  is the current term, and  $f_w$  is wind-wave term. OCN RVL products contain the  $f_{Dc}$  term and the  $f_{Dp}$  term. The result obtained by subtracting  $f_{Dp}$  from  $f_{Dc}$  is the Doppler centroid anomaly  $f_{Dca}$ . To obtain the geophysical components, the additional components of the non-geophysical Doppler term need to be removed first. The flowchart to correct DCA and the subsequent inversion is detailed in Figure 2. Each step is described in the next section.

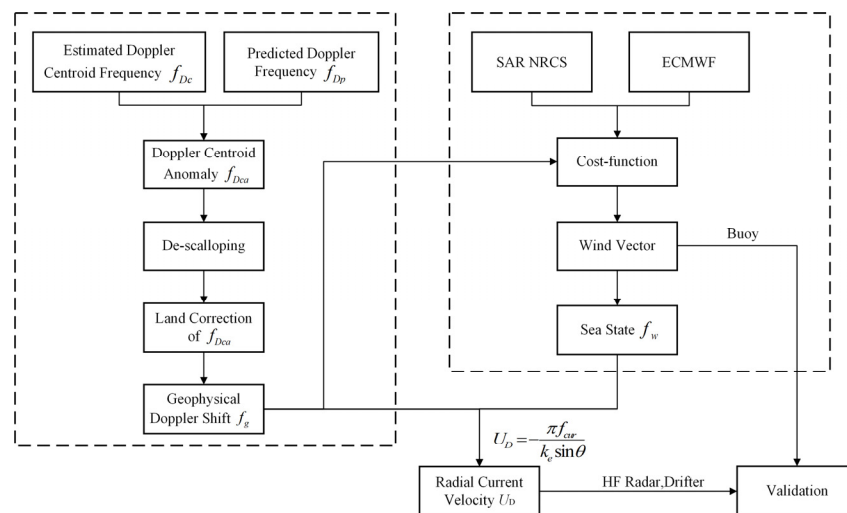


**Figure 2.** Flowchart of DCA correction and inversion of wind and current velocity as well as the validation.

## 3. Results and Discussions

### 3.1. DCA Correction

Figure 3 displays a SAR image acquired in the Gulf of Maine on 10 August 2019, by S-1A. In Figure 3a, the NRCS acquired by VV polarization is depicted, while Figure 3b illustrates the estimated Doppler centroid frequency. This image is collected by the ascending

orbit with the satellite flying from the south to the north, and a detrend pattern of NRCS is clear from the left (near-range) to the right (far-range) of this plot. It exhibits a complex ocean scene, particularly close to the land. For instance, dark spots corresponding to low radar backscatter are observed in the upper left corner of the image, possibly due to an oil spill or a low-wind area. A cluster of bright targets is observed near the Grand Manan Island at longitude of 67.5° W and latitude of 44.5° N. In addition to NRCS, the Doppler centroid annotated in the S-1 level-2 product is given in Figure 3b. The value of the Doppler centroid over the sea surface differs from that over the land. A couple of outlier patterns are clear, including the periodic band along the flight direction and the non-zero values over the land.

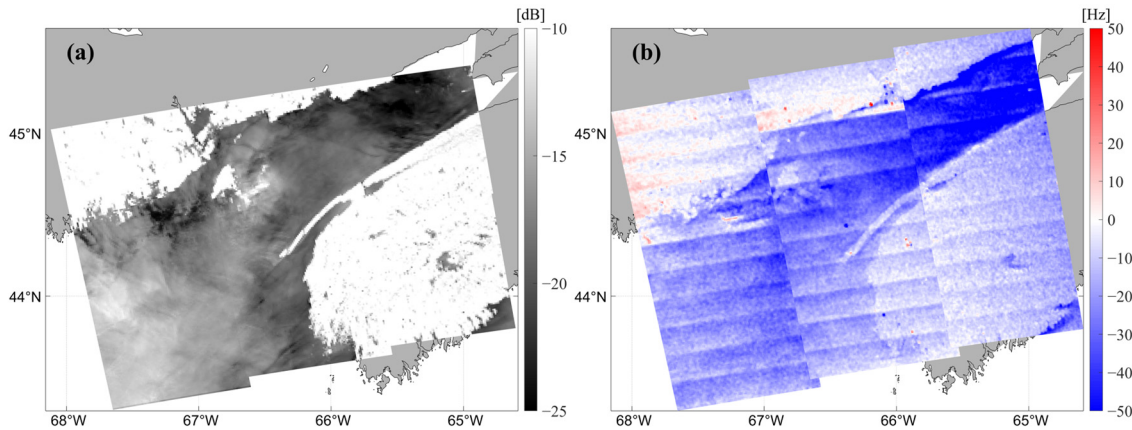


**Figure 3.** Map of an SAR image acquired over the Gulf of Maine on 10 August 2019 for (a) NRCS at VV polarization and (b) SAR-estimated Doppler centroid.

Figure 4a presents the predicted (geometric) Doppler frequency. After subtracting the predicted Doppler frequency from the SAR-estimated Doppler frequency, the outliers possibly caused by environmental factors still persist. To mitigate the impact, we initially employ the  $3\sigma$  method to identify and eliminate these anomalies along both the azimuth and range directions for each swath. The  $3\sigma$  method, as defined in Equation (4), flags a pixel as an outlier when its value deviates from the median by more than three standard deviations (with the median and standard deviation calculated in either the range or azimuth directions). For each pixel in the image domain, it is considered as an outlier if satisfying the following condition:

$$|x - \tilde{x}_{ra}| > 3\sigma_{ra} \text{ or } |x - \tilde{x}_{az}| > 3\sigma_{az} \tag{4}$$

where ‘ $x$ ’ denotes the SAR-estimated Doppler centroid,  $\tilde{x}$  is the median value, and ‘ $\sigma$ ’ is the standard deviation along the range or azimuth direction, respectively. The Doppler centroid values of the outlier pixels are replaced by the average over the surrounding  $25 \times 25$  pixels.

Figure 4b exhibits the Doppler centroid anomaly after the removal of outliers.

The undulating pattern observed in each sub-strip in Figure 4b, known as a burst, is called  $f_{sca}$ , and it exhibits distinct periodic changes in the azimuthal direction. There are currently two methods: (1) removing trend signals in the spatial domain; (2) removing them in the frequency domain through Fourier transform [23]. This study uses the first method. Each sub-strip is first averaged in the range direction (the solid blue line in Figure 5a), and the trend in the azimuth signal is removed by fitting and subtracting a third-order polynomial (the dashed blue line in Figure 5a), and a periodically changing signal is then obtained (the solid black line in Figure 5a). We assume that this is the scallop signal, and then have it removed from  $f_{sca}$  for each sub-swath. Figure 5b shows the Doppler centroid anomaly after scalloping correction. Notably, since 24 June 2020, the S-1 Instrument Processing Facility version 3.30 (IPF) incorporates an azimuth scalloping correction, resulting in a threefold reduction in modulation [24]. We have checked that the

products collected after this IPF mostly have a subtle scalloping effect. Nevertheless, the above mentioned algorithm is consistently implemented for all products despite the fact that this procedure might have a negligible impact on the scalloping removal.

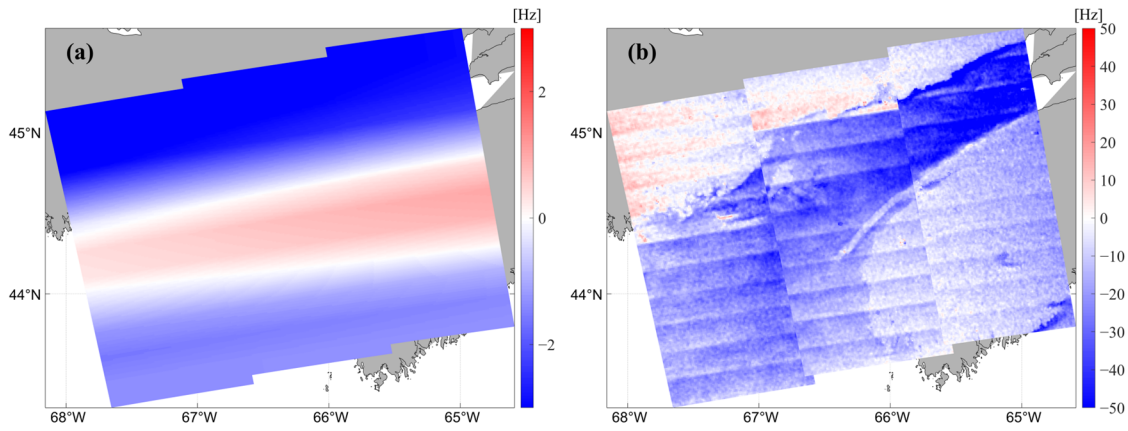


**Figure 4.** Map of (a) the predicted (geometric) Doppler centroid and (b) the obtained Doppler centroid anomaly after subtracting the predicted Doppler centroid and the suppression of outliers.

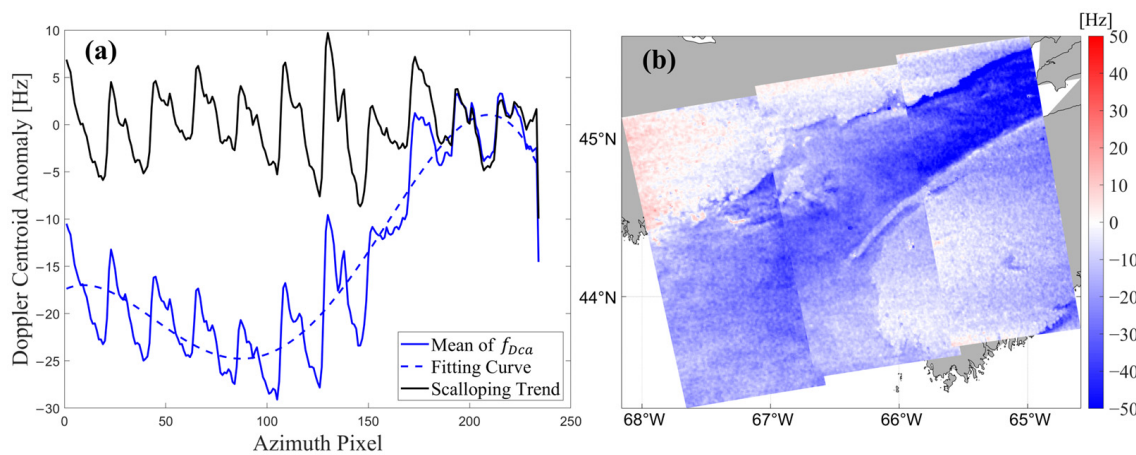


**Figure 5.** (a) Demonstration of de-scalloping of DCA. The solid curve in blue denotes the averaged DCA along the azimuth direction, and the dashed line in blue is the third-order polynomial fit. The black solid curve is the scalloping signal to be removed for each sub-swath. (b) The map of DCA after scalloping corrections.

The error in antenna electronic miss-pointing  $f_{em}$  arises from the radar antenna’s directional deviation and orbital information discrepancies, leading to a deviation between the actual and theoretical beam-pointing angles. Typically, land is employed as reference data for correcting the DCA of 0. This correction is achieved utilizing the pixel points on land as shown in Figure 6a. The averaged DCA along the range direction is illustrated in Figure 4b for each sub-swath. Upon subtracting this component, what persists is the geophysical Doppler shift. After eliminating the non-geophysical factors, the remaining (geophysical) Doppler shift is directly linked to the ocean surface velocity. This velocity is primarily influenced by the orbital velocities of sea surface waves, establishing the connection between the Doppler shift and surface wind [13], as well as surface currents [15]. Consequently, it becomes essential to eliminate this sea-state influence  $f_w$  to extract the current-related velocity.

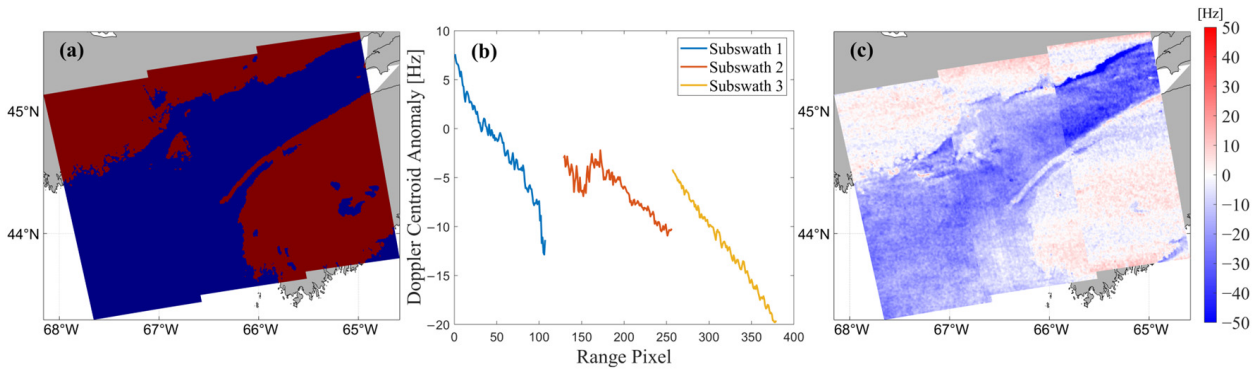


**Figure 6.** (a) Land coverage in the Gulf of Maine (red mask for land covered area); (b) radial variation of Doppler centroid anomaly on land; (c) land-corrected Doppler anomaly.

### 3.2. Wind Retrieval and Validation

Bayesian methods were initially introduced and applied for scatterometer measurements [25]. The utilization of a variational approach for SAR wind field inversion was first suggested by [26], wherein the NRCS is employed alongside external wind speed and direction, typically acquired from numerical weather prediction (NWP) or reanalysis, as prior information. The reference [12] emphasized that incorporating Doppler shifts, in addition to backscatter and background winds, enhances inversion outcomes compared to Bayesian methods that solely consider NRCS. This improvement is particularly notable in cases where the background wind vector deviates from the actual wind vector, leading to a significant enhancement in wind direction accuracy.

The inversion scheme used in this study is based on the premise that these three variables are weakly correlated [27], and can be applied independently to each wind cell. It is assumed that the background wind vector and the true wind vector errors follow a Gaussian normal distribution and are uncorrelated. Here, we combine NRCS, the background wind field, and the Doppler information to construct the cost function of SAR sea surface wind retrieval algorithm, as in Equation (5), and the sea surface wind vector solution is calculated by searching for the minimum value of the cost function.

$$J = \left( \frac{\sigma(u, v) - \sigma_{obs}}{\Delta\sigma} \right)^2 + \left( \frac{u - u_m}{\Delta u} \right)^2 + \left( \frac{v - v_m}{\Delta v} \right)^2 + \left( \frac{f_D - f_{Dm}}{\Delta f_D} \right)^2 \quad (5)$$

where  $(u, v)$  is the wind vector space,  $\sigma(u, v)$  is the predicted NRCS using CMOD7 for a given  $(u, v)$ .  $\sigma_{obs}$  is SAR-observed NRCS.  $(u_m, v_m)$  is the a priori wind vector.  $f_D$  is the SAR-observed DCA, and  $f_{Dm}$  is the prediction of the CDOP for a given  $(u, v)$ .  $\Delta u, \Delta v$  are the Gaussian standard deviation errors for model wind vector, and  $\Delta\sigma, \Delta f_D$  are the Gaussian standard deviation errors for the NRCS and the Doppler shift.

To demonstrate the contribution of each term in the cost function, we assume a true wind speed of 7 m/s at a wind direction of  $60^\circ$ , an incidence angle of  $30^\circ$ , and an a priori wind speed of 12 m/s with a wind direction of  $30^\circ$ . The Gaussian standard deviation errors for each term are considered as constants based on the radiometric accuracy of the S-1 SAR, with values of  $\Delta\sigma = 0.1\sigma_{obs}$  and  $\Delta f_D = 10$  Hz and  $\Delta u = \Delta v = \sqrt{3}$  m/s, respectively. Substituting these terms into the cost function, a space of wind speed (0–40 m/s) and wind direction (0– $360^\circ$ ) are calculated. The cost function results are influenced by the NRCS term, Doppler term, and a priori model term as shown in Figure 7. The dark color indicates a lower cost function value, suggesting a more likely wind vector solution. When considering only NRCS or DCA for the cost function, multiple minima (black curves) indicate an under-constrained problem. The red ‘□’ represents the true wind vector, while ‘×’ marks the local minima of the cost function. When accounting for the NRCS term and the background wind vector term as in Figure 7d, the inversion results for wind speed and wind direction are 6.8 m/s and  $41^\circ$ , respectively. With the addition of Doppler information,

the inversion yields a wind speed of 7.2 m/s and a wind direction of 54°, signifying a significant improvement in direction accuracy, as shown in Figure 7f.

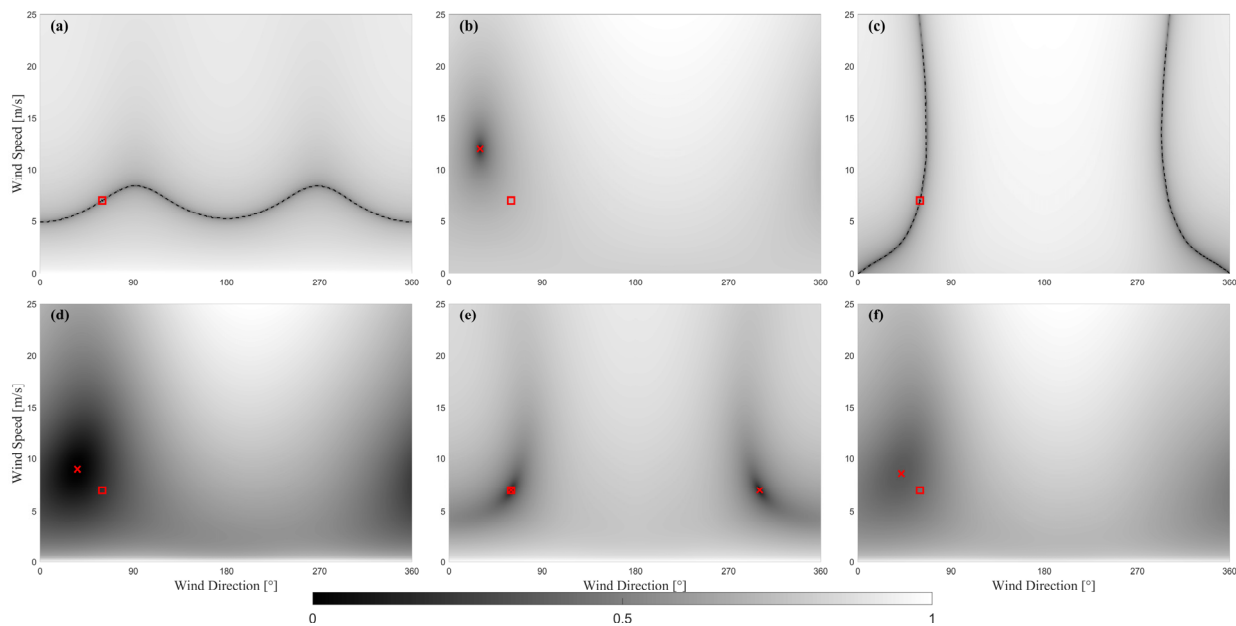


**Figure 7.** Illustration of contribution of each term in the cost function. (a) NRCS term; (b) a priori (model) term; (c) Doppler term; (d) NRCS and model; (e) NRCS and Doppler; (f) NRCS, Doppler, and model. ‘□’ indicates the true wind and ‘×’ indicates the local minima for cost function.

According to Equation (5), we combine radar NRCS, background wind field, and Doppler information into the cost function. Figure 8 shows the comparison between the retrieved wind vector with DCA and the wind vector measured by buoys. The incorporation of the Doppler centroid anomaly significantly enhances the accuracy of both wind speed and direction, although the standard deviation remains unchanged (see Table 1). This might be attributable to the fact that the CDOP was developed using global sea surfaces, primarily encompassing open oceans. In these open oceanic regions, the influence of ocean currents on Doppler centroid anomalies is notably smaller compared to that of winds. However, in coastal areas, where currents and waves play a more substantial role in Doppler centroid anomalies relative to winds, the improvement in wind field inversion results is not as pronounced. A comparison with in situ data underscores the Bayesian method’s consistency and practical efficacy in wind field inversion.

The retrieved wind speed gives an overall good performance with a correlation coefficient of 0.931, a mean bias of 0.33 m/s, and a root-mean-square error (RMSE) of 1.45 m/s. For the wind direction, the overall correlation coefficient of wind direction reaches 0.661 with a bias of 6.94° and a RMSE of 35.74°. The empty circles correspond to the cases where the wind speed is lower than 4m/s. It can be clearly seen that when the wind speed is lower than 4 m/s, the error of the wind direction increases significantly, which might be due to the weaker sensitivity of GMF to low wind speed. The scatter index (SI) also greatly decreases at higher wind speeds. These metrics improve greatly when calculating the deviation and standard deviation of wind direction excluding the cases of wind speeds of less than 4 m/s as annotated. By comparison, the performance metrics of wind retrieval based on NRCS plus model winds without input of Doppler information is listed in Table 1. The bias is 0.34 m/s and 7.25° for wind speed and direction, respectively, with the RMSE values being 1.45 m/s and 35.84°. While the improvement may not be substantial, the slightly improved bias and RMSE still suggest a degree of accuracy in our wind retrieval.

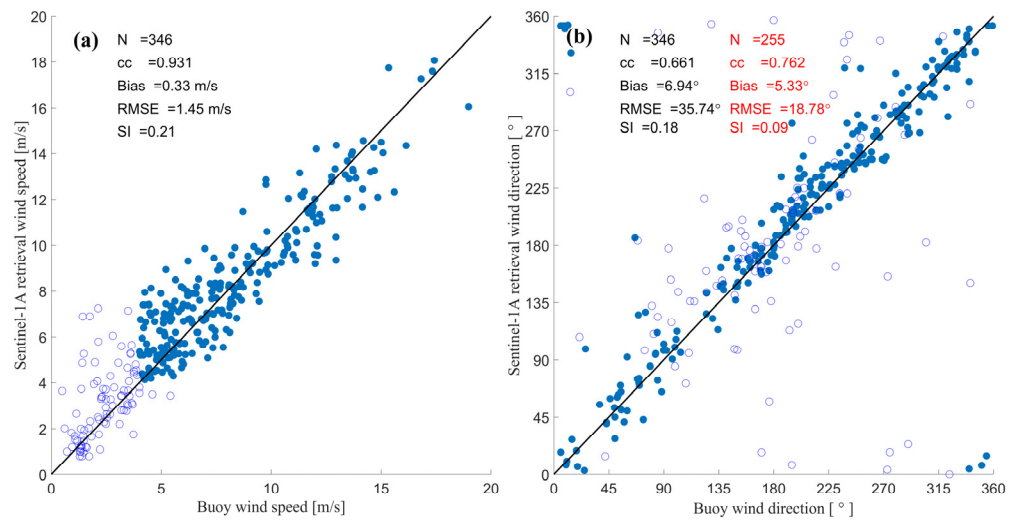


**Figure 8.** Comparison of retrieved winds and buoy-measured winds for (a) wind speed and (b) wind direction. The performance metrics are annotated in each plot. The metrics in red in subplot (b) correspond to the results for wind speed higher than 4 m/s. The empty dots correspond to the points of wind speed lower than 4m/s.

**Table 1.** Performance comparison of different cost functions.

Variable	Metrics	NRCS + Model	NRCS + Model + Doppler
Wind speed	Bias [m/s]	0.34	0.33
	RMSE [m/s]	1.45	1.45
Wind direction	Bias [°]	7.25	6.94
	RMSE [°]	35.84	35.74

### 3.3. Current Retrieval and Validation

As introduced above, Doppler shift can be viewed as the radar’s movement relative to the sea surface, composed of the platform motion, the sea surface wind field, and the motion induced by waves, as well as the influence of currents. The total contribution can be formulated as

$$f_{cur} = f_D - f_w \tag{6}$$

where  $f_{cur}$  denotes the residual Doppler shift associated with the surface radial current velocity.  $f_D$  is the geophysical Doppler shift after correction, which is used for wind retrieval in Equation (5).  $f_w$  is the sea-state contribution that needs to be removed from the corrected geophysical Doppler to obtain the surface current component.  $f_w$  is estimated using the retrieved wind speed and direction with the CDOP model. The surface current velocity is related to the residual Doppler shift by

$$U_D = -\frac{\pi f_{cur}}{k_e \sin \theta} \tag{7}$$

where  $k_e$  is the incident radar wavenumber.  $U_D$  is assumed to be the line-of-sight velocity of the ocean surface current.

Figure 9a depicts the radial current velocity of the SAR scene acquired on 26 September 2019. The red region in the figure represents surface velocity directed towards the satellite range line, indicating the current flowing northeastward. Beyond the Gulf Stream, the current velocity appears relatively uniform, ranging from 0.1 to 0.5 m/s, while within the Gulf Stream, velocities generally exceed 1 m/s. To validate the currents obtained through the above method, the spatial map of surface currents observed by HFR is plotted for comparison. In Figure 9b, the currents observed by HFR at 23:00 on the same day are

presented, revealing a distribution similar to the SAR-retrieved radial current velocity. Both images capture the Gulf Stream, where current velocities can reach 1.5 m/s. Figure 9c illustrates the comparison between the observed currents from the drift buoy projecting onto the radial direction of SAR observations and the inverted currents. In most cases, there is a strong consistency between the two datasets. However, due to potential significant variations in currents throughout the day, some outliers may be present. The overall correlation coefficient is 0.87, and after excluding individual outliers, the correlation coefficients and the metrics improve greatly. For example, the bias between the two sets of data is approximately 0.02 m/s. Another point worth noting is that the abnormally larger current velocity reaching up to 2 m/s observed by the drifters might be due to errors in the products. The overall RMSE of 0.32 m/s cannot be ignored; this might be due to the relatively long collocation time window of a duration within 3 h. Assuming a current velocity of 0.5 m/s, it will propagate out a distance of 5.4 km, which is larger than the spatial collocation criteria. To diagnose the potential uncertainty, we divided the data points into two groups: one with a collocation time within 1 h and the other with a collocation time longer than 1 h. The respective RMSEs of the retrieved current velocity component for these two groups are 0.28 m/s and 0.33 m/s, implying the impact of collocation time. Note that the drifter current measurements are available every 6 h, which may also induce additional uncertainties.

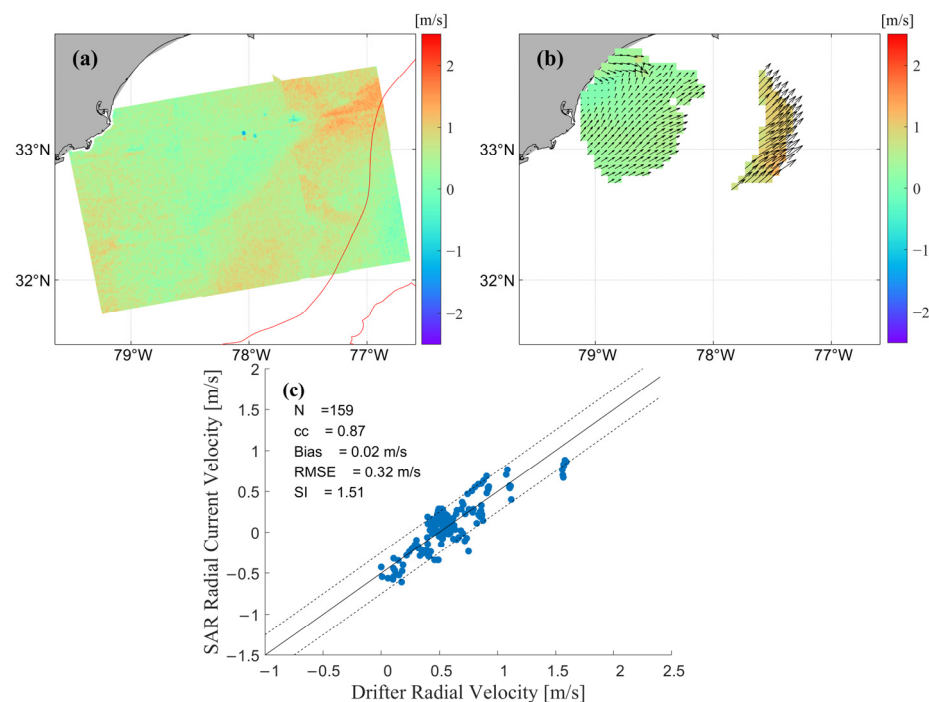


**Figure 9.** Comparison of retrieved oceanic current with reference dataset. (a) SAR-derived radial current velocity on 26 September 2019 overlapped with the trajectory of drifters (solid line in red). (b) Sea surface current velocity vector observed by HF radar on 26 September 2019. (c) Pointwise comparison of drifter measured radial velocity versus SAR-derived current velocity with the comparison metrics annotated in the plot. Note that all the collocation pairs between SAR and drifters are included in panel (c) to generate the scatter plot.

#### 4. Summary

In this study, we take advantage of multiple SAR images over the North Atlantic to investigate the joint retrieval performance of wind vector and line-of-sight current velocity using a Bayesian approach. To achieve this purpose, the NRCS and Doppler information of SAR images, representing backscattering magnitude and phase of radar return, are combined in the inversion scheme, along with a priori wind information. A series of correction steps are first carried out to obtain the geophysical component of the

Doppler centroid from SAR estimates. This includes the removal of scalloping effect and antenna miss-pointing based on land coverage. The performance of the inversion scheme combining NRCS, DCA, and the model winds is then evaluated with respect to in situ buoy measurements. The metrics indicate a slight improvement in comparison to the inversion results with the input of Doppler information.

For sea surface current inversion, the study introduces the use of the CDOP model to estimate and correct Doppler frequency shifts induced by sea surface wind and waves. This correction mechanism is found to enhance the accuracy of ocean current inversion. The results highlight the consistency of velocities obtained through S-1 inversion with high-frequency ground-based radar observations. Furthermore, the spatial distribution characteristics of ocean currents can be effectively derived through this innovative integration of S-1 data, offering valuable insights into oceanographic dynamics.

The Doppler information of SAR images can certainly play a role in relevant geophysical fields [27]. However, there are some deviations in certain regions that can be attributed to a couple of reasons. For example, the partial land coverage across the swath width may result in inconsistency in Doppler corrections. In addition, the DCA included in the cost function of the inversion scheme combines the wind and current contribution, which might lead to a bias in the retrieval results. Thus, how to take into account this combination and a possible extension over the polar regions will be the focus of our following work [28].

**Author Contributions:** Conceptualization, H.L.; Formal analysis, J.S.; Investigation, H.L. and W.L.; Writing—original draft, J.S. and H.L.; Writing—review & editing, H.L., W.L. and Y.H.; Supervision, Y.H.. All authors have read and agreed to the published version of the manuscript.

**Funding:** This research was funded by the National Science Foundation of China under grants 42027805 and 42006163.

**Institutional Review Board Statement:** Not applicable.

**Informed Consent Statement:** Not applicable.

**Data Availability Statement:** Copernicus Sentinel-1 data are used and are publicly available via <https://scihub.copernicus.eu/> (accessed on 10 November 2023), the buoy winds are available via <https://www.ndbc.noaa.gov/> (accessed on 10 November 2023), the high-frequency radar current measurements are available via <https://hfrnet-tds.ucsd.edu/> (accessed on 10 November 2023), and the drifter current velocity products are available via <https://www.aoml.noaa.gov/phod/gdp/index.php> (accessed on 10 November 2023).

**Acknowledgments:** We would like to thank ESA for providing Sentinel-1 data, NDBC for the buoy winds data, the Scripps Institution of Oceanography for the HF radar products, and NOAA for the drifter dataset.

**Conflicts of Interest:** The authors declare no conflicts of interest.

## References

1. Durand, M.; Fu, L.-L.; Lettenmaier, D.P.; Alsdorf, D.E.; Rodriguez, E.; Esteban-Fernandez, D. The surface water and ocean topography mission: Observing terrestrial surface water and oceanic submesoscale eddies. *Proc. IEEE* **2010**, *98*, 766–779. [[CrossRef](#)]
2. Bourassa, M.A.; Meissner, T.; Ceroveck, I.; Chang, P.S.; Dong, X.L.; De Chiara, G.; Donlon, C.; Dukhovskoy, D.S.; Elya, J.; Fore, A.; et al. Remotely Sensed Winds and Wind Stresses for Marine Forecasting and Ocean Modeling. *Front. Mar. Sci.* **2019**, *6*, 443. [[CrossRef](#)]
3. He, Y.; Liu, B.; Zhang, B.; Cheng, Z.; Qiu, Z. Overview on satellite remote-sensing methods for sea-surface-current measurement. *Guangxi Sci.* **2015**, *22*, 294–300. [[CrossRef](#)]
4. Stoffelen, A.; Anderson, D. Scatterometer data interpretation: Estimation and validation of the transfer function CMOD4. *J. Geophys. Res. Ocean.* **1997**, *102*, 5767–5780. [[CrossRef](#)]
5. Ju-Hong, Z.; Ming-Sen, L.; De-Lu, P.; Zheng-Hua, C.; Le, Y. A unified C-band and Ku-band GMF determined by using neural network approach. *Acta Oceanol. Sin.* **2008**, *30*, 23–28. [[CrossRef](#)]
6. Zecchetto, S.; De Biasio, F.; della Valle, A.; Quattrocchi, G.; Cadau, E.; Cucco, A. Wind Fields From C- and X-Band SAR Images at VV Polarization in Coastal Area (Gulf of Oristano, Italy). *IEEE J. Sel. Top. Appl. Earth Observ. Remote Sens.* **2016**, *9*, 2643–2650. [[CrossRef](#)]

7. Du, Y.; Dong, X.; Jiang, X.; Zhang, Y.; Zhu, D.; Sun, Q.; Wang, Z.; Niu, X.; Chen, W.; Zhu, C. Ocean Surface Current multiscale Observation Mission (OSCOM): Simultaneous measurement of ocean surface current, vector wind, and temperature. *Prog. Oceanogr.* **2021**, *193*, 102531. [[CrossRef](#)]
8. Qiu, B.; Chen, S.; Klein, P.; Torres, H.; Wang, J.; Fu, L.; Menemenlis, D. Reconstructing Upper-Ocean Vertical Velocity Field from Sea Surface Height in the Presence of Unbalanced Motion. *J. Phys. Oceanogr.* **2020**, *50*, 55–79. [[CrossRef](#)]
9. Keller, W.; Plant, W.; Valenzuela, G. Observation of breaking ocean waves with coherent microwave radar. In *Wave Dynamics and Radio Probing of the Ocean Surface*; Springer: Boston, MA, USA, 1986; pp. 285–293. [[CrossRef](#)]
10. Horstmann, J.; Koch, W.; Lehner, S.; Tonboe, R. Ocean winds from RADARSAT-1 ScanSAR. *Can. J. Remote Sens.* **2002**, *28*, 524–533. [[CrossRef](#)]
11. Monaldo, F.; Thompson, D.; Beal, R.; Pichel, W.; Clemente-Colon, P. Comparison of SAR-derived wind speed with model predictions and ocean buoy measurements. *IEEE Trans. Geosci. Remote Sens.* **2001**, *39*, 2587–2600. [[CrossRef](#)]
12. Mouche, A.; Collard, F.; Chapron, B.; Dagestad, K.; Guitton, G.; Johannessen, J.; Kerbaol, V.; Hansen, M. On the Use of Doppler Shift for Sea Surface Wind Retrieval From SAR. *IEEE Trans. Geosci. Remote Sens.* **2012**, *50*, 2901–2909. [[CrossRef](#)]
13. Chapron, B.; Collard, F.; Ardhuin, F. Direct measurements of ocean surface velocity from space: Interpretation and validation. *J. Geophys. Res. Ocean.* **2005**, *110*, 17. [[CrossRef](#)]
14. Hansen, M.W.; Collard, F.; Dagestad, K.F.; Johannessen, J.A.; Fabry, P.; Chapron, B. Retrieval of Sea Surface Range Velocities From Envisat ASAR Doppler Centroid Measurements. *IEEE Trans. Geosci. Remote Sens.* **2011**, *49*, 3582–3592. [[CrossRef](#)]
15. Rouault, M.J.; Mouche, A.; Collard, F.; Johannessen, J.A.; Chapron, B. Mapping the Agulhas Current from space: An assessment of ASAR surface current velocities. *J. Geophys. Res. Ocean.* **2010**, *115*, 14. [[CrossRef](#)]
16. Kang, K.; Kim, D.j.; Kim, S.H.; Moon, W. Doppler Velocity Characteristics During Tropical Cyclones Observed Using ScanSAR Raw Data. *IEEE Trans. Geosci. Remote Sens.* **2016**, *54*, 2343–2355. [[CrossRef](#)]
17. Bao, Q. System Design and Simulation of Doppler Scatterometer—Wide Swath Ocean Surface Current Measurement. Department of Electromagnetic Field and Microwave Technology. Ph.D. Thesis, University of Chinese Academy of Sciences, Beijing, China, 2015.
18. Moiseev, A.; Johannessen, J.A.; Johnsen, H. Towards Retrieving Reliable Ocean Surface Currents in the Coastal Zone From the Sentinel-1 Doppler Shift Observations. *J. Geophys. Res. Ocean.* **2022**, *127*, e2021JC018201. [[CrossRef](#)]
19. Martin, A.C.; Gommenginger, C.P.; Jacob, B.; Staneva, J. First multi-year assessment of Sentinel-1 radial velocity products using HF radar currents in a coastal environment. *Remote Sens. Environ.* **2022**, *268*, 112758. [[CrossRef](#)]
20. Eyre, J.R.; English, S.J.; Forsythe, M. Assimilation of satellite data in numerical weather prediction. *Part I Early Years. Q. J. R. Meteorol. Soc.* **2020**, *146*, 49–68. [[CrossRef](#)]
21. Elipot, S.; Lumpkin, R.; Perez, R.C.; Lilly, J.M.; Early, J.J.; Sykulski, A.M. A global surface drifter data set at hourly resolution. *J. Geophys. Res. Oceans* **2016**, *121*, 2937–2966. [[CrossRef](#)]
22. Stoffelen, A.; Verspeek, J.A.; Vogelzang, J.; Verhoef, A. The CMOD7 geophysical model function for ASCAT and ERS wind retrievals. *IEEE J. Sel. Top. Appl. Earth Observ. Remote Sens.* **2017**, *10*, 2123–2134. [[CrossRef](#)]
23. Elyouncha, A.; Eriksson, L.E.B.; Johnsen, H.; Ulander, L.M.H. Using Sentinel-1 Ocean Data for Mapping Sea Surface Currents Along the Southern Norwegian Coast. In *Proceedings of the IGARSS 2019—2019 IEEE International Geoscience and Remote Sensing Symposium, Yokohama, Japan, 28 July–2 August 2019*; pp. 8058–8061. [[CrossRef](#)]
24. Hajduch, G.; Vincent, P.; Piantanida, R.; Recchia, A.; Franceschi, N.; Schmidt, K.; Johnsen, H.; Mouche, A.; Grouazel, A.; Collard, F. *Sentinel-1 A and B Annual Performance Report for 2020*; Tech. Rep. MPC-0504; Mission Performance Center, ESA: Paris, France, 2021.
25. Hoffman, R.; Leidner, S.; Henderson, J.; Atlas, R.; Ardizzone, J.; Bloom, S. A two-dimensional variational analysis method for NSCAT ambiguity removal: Methodology, sensitivity, and tuning. *J. Atmos. Ocean. Technol.* **2003**, *20*, 585–605. [[CrossRef](#)]
26. Portabella, M.; Stoffelen, A.; Johannessen, J.A. Toward an optimal inversion method for synthetic aperture radar wind retrieval. *J. Geophys. Res. Ocean.* **2002**, *107*, 1–13. [[CrossRef](#)]
27. Elyouncha, A.; Eriksson, L.E.; Broström, G.; Axell, L.; Ulander, L.H. Joint retrieval of ocean surface wind and current vectors from satellite SAR data using a Bayesian inversion method. *Remote Sens. Environ.* **2021**, *260*, 112455. [[CrossRef](#)]
28. Li, X.-M.; Qin, T.; Wu, K. Retrieval of Sea Surface Wind Speed from Spaceborne SAR over the Arctic Marginal Ice Zone with a Neural Network. *Remote Sens.* **2020**, *12*, 3291. [[CrossRef](#)]

**Disclaimer/Publisher’s Note:** The statements, opinions and data contained in all publications are solely those of the individual author(s) and contributor(s) and not of MDPI and/or the editor(s). MDPI and/or the editor(s) disclaim responsibility for any injury to people or property resulting from any ideas, methods, instructions or products referred to in the content.